Ultrasound in Med. & Biol., Vol. 39, No. 6, pp. 1075–1086, 2013

0301-5629/$ - see front matter

http://dx.doi.org/10.1016/j.ultrasmedbio.2013.01.008

● *Original Contribution*

SONOPORATION AS A CELLULAR STRESS: INDUCTION OF MORPHOLOGICAL REPRESSION AND DEVELOPMENTAL DELAYS

XIAN CHEN,* JENNIFER M. F. WAN,† and ALFRED C. H. YU*

*Medical Engineering Program, University of Hong Kong, Pokfulam, Hong Kong SAR, China; and †School of Biological Sciences, University of Hong Kong, Pokfulam, Hong Kong SAR, China

(*Received* 24 *October* 2012; *revised* 8 *January* 2013; *in final form* 15 *January* 2013)

Abstract—For sonoporation to be established as a drug/gene delivery paradigm, it is essential to account for the biological impact of this membrane permeation strategy on living cells. Here we provide new insight into the cellular impact of sonoporation by demonstrating *in vitro* that this way of permeating the plasma membrane may inadvertently induce repressive cellular features even while enhancing exogenous molecule uptake. Both suspension-type (HL-60) and monolayer (ZR-75-30) cells were considered in this investigation, and they were routinely exposed to 1-MHz pulsed ultrasound (pulse length, 100 cycles; pulse repetition frequency, 1 kHz; exposure period, 60 s) with calibrated field profile (spatial-averaged peak negative pressure, 0.45 MPa) and in the presence of microbubbles (cell:bubble ratio, 10:1). The post-exposure morphology of sonoporated cells (identified as those with calcein internalization) was examined using confocal microscopy, and their cell cycle progression kinetics were analyzed using flow cytometry. Results show that for both cell types investigated, sonoporated cells exhibited membrane shrinkage and intra-cellular lipid accumulation over a 2-h period. Also, as compared with normal cells, the deoxyribonucleic acid synthesis duration of sonoporated cells was significantly lengthened, indicative of a delay in cell cycle progression. These features are known to be characteristics of a cellular stress response, suggesting that sonoporation indeed constitutes as a stress to living cells. This issue may need to be addressed in optimizing sonoporation for drug/gene delivery purposes. On the other hand, it raises opportunities for developing other therapeutic applications *via* sonoporation. (E-mail: alfred.yu@hku.hk)

Key Words: **Sonoporation, Cellular stress, Membrane shrinkage, Lipid accumulation, DNA synthesis delay.**

INTRODUCTION

Sonoporation, which refers to membrane permeation generated through acoustic cavitation means as confirmed by experimental data (Qiu et al. 2010), has spurred significant scientific interest since its initial demonstration because of its potential in facilitating uptake of drugs and genes into living cells (Frenkel 2008; Miller et al. 2002; Pua and Zhong 2009). This biophysical phenomenon is often realized with the use of synthetic microbubble, which serve as artificial cavitation nuclei (Sirsi and Borden 2009), and it has been reported that precise control of the permeation site is achievable through meticulous instrumentation design (Zhou et al. 2012). With the increasing level of technical maturity in realizing sonoporation, there is a growing interest in gaining a deeper understanding of the cellular response related to this biophysical phenomenon. One key biological aspect of interest is whether sonoporated cells can maintain homeostasis (Campbell and Prausnitz 2007), given that the plasma membrane is mechanically wounded and morphological events like membrane blebbing may occur on an immediate basis (Schlicher et al. 2010). From a drug/gene delivery standpoint, it is important to address this fundamental question because preservation of cell viability is generally of high priority in many applications (except, perhaps, for cancer treatment).

For sonoporated cells to remain viable, membrane resealing is unarguably crucial, and this is known to take place within seconds after exposure through a calcium ion (Ca^{2+})-mediated mechanism that presumably involves patching of the permeated site with intracellular vesicles (Hassan et al. 2010; Zhou et al. 2008). Nevertheless, the occurrence of membrane resealing does not necessarily imply that sonoporated cells would maintain viability in the long run (Feril and Kondo 2004), as various anti-proliferative effects including

Address correspondence to: Alfred C. H. Yu, Medical Engineering Program, University of Hong Kong, Pokfulam, Hong Kong SAR, China. E-mail: alfred.yu@hku.hk

apoptosis (Miller and Dou 2009), cell cycle arrest (Zhong et al. 2011) and suppression of clonogenicity (Karshafian et al. 2010) may arise many hours after exposure. This signifies that sonoporation may essentially pose a stress to living cells, and it may represent a confounding factor when using sonoporation for drug/gene delivery purposes. Indeed, recent statistics have prompted reservations over whether sonoporation can on its own serve as an efficient drug delivery strategy in which large drug payloads can be delivered into cells without affecting cell viability in tandem (Liu et al. 2012).

To counteract the repressive impact of sonoporation and, in turn, maintain cell viability, cytoprotection strategies would likely need to be administered in parallel. Post-exposure intra-cellular Ca^{2+} chelation is one particular solution that has been considered (Hutcheson et al. 2010), and it is intended to act against the Ca^{2+} influx triggered by sonoporation (Fan et al. 2010; Kumon et al. 2009; Park et al. 2010; Tsukamoto et al. 2011). Inclusion of pluronic polymers as part of the drug payload has also been proposed to mitigate sonoporation-induced cytotoxic effects (Chen et al. 2006; Mehier-Humbert et al. 2009). However, without a proper account of the mechanistic pathways involved in the sonoporation-induced stress response, it would be futile to pursue further development of these strategies for use beyond the initial proof-of-principle stage, as other unintended bioeffects may be overlooked.

In this investigation, it is our aim to understand better how sonoporation may be acting as a stress on biological cells so as to facilitate optimization of the sonoporation-mediated drug/gene delivery paradigm. Specifically, we seek to obtain insight into the cytotoxic impact of sonoporation by gaining new perspectives on anti-proliferative characteristics that may emerge within sonoporated cells after membrane resealing has occurred. Our investigation is guided by two research hypotheses. First, because sonoporation involves physical wounding of cell membrane and subsequent resealing through intra-cellular vesicle patching, the morphology of sonoporated cells under recovery must inherently differ from that of normal viable cells. Second, as part of the stress response, the cell cycle progression kinetics of sonoporated cells must be modified from those of normal cells. As such, this work has focused on elucidating repressive morphological features and developmental disturbances that may arise in sonoporated cells over time as they undergo recovery after membrane resealing.

METHODS

Preparation of cell lines

The morphology and developmental behavior of sonoporated cells have been investigated for both cell suspensions and monolayers. The HL-60 leukemia cell line (CCL-240; American Type Culture Collection [ATCC], Manassas, VA, USA) was used as the suspension model, whereas the ZR-75-30 breast carcinoma cell line (CRL-1504; ATCC) was used as the attached cell model. Note that cancerous cell lines have been chosen for this study in view of their immortality and natural resistance to proapoptotic stress (these prosurvival characteristics would effectively serve as part of the experimental control for our investigation, which aims to demonstrate the repressive impact of sonoporation). Both cell lines were routinely cultured in Roswell Park Memorial Institute 1640 medium (R8758; Sigma–Aldrich, St. Louis, MO, USA) and were supplemented with 10% fetal bovine serum (FBS, 30-2020; ATCC). The cell culture incubator was kept at 37°C with 5% carbon dioxide (CO_2). Asynchronous and exponential cell growth was maintained by monitoring cell density to ensure that it did not exceed 10^6 cells/mL (for HL-60) or 10^7 cells in an 80-cm^2 culture flask (for ZR-75-30).

One day before the experiment, the cells were fed with fresh medium. They were then extracted and transferred to custom-made chamber well slides, each of which was essentially an acrylic slab (80 mm in length, 30 mm in width, 5 mm in height) with a cylindrical well bore in the center (12-mm well diameter, 0.6-mL working volume). Note that prior to extraction, the ZR-75-30 cells were first resuspended using 0.25% trypsin (59428C; Sigma–Aldrich). Also, each chamber well slide was sealed respectively with a 0.13-mm-thick coverslip (Bellco Glass, Vineland, NJ, USA) at the bottom surface and a 0.18-mm-thick HybriWell cover (S24730; Invitrogen, Carlsbad, CA, USA) at the top surface. Transfer of cells into the chamber well was facilitated through two filling ports on the HybriWell cover, and these ports were patched with seal tabs (A18211; Invitrogen) after the transfer to ensure secured sealing.

In this work, a population of 1.2×10^6 cells was used for each sample of HL-60 cell suspension and for ZR-75-30 cell samples that underwent post-exposure flow cytometry assays. For ZR-75-30 cells used in confocal microscopy analysis, a smaller population of 10^4 cells was used in each sample to allow cells to reattach and form a cell monolayer on the chamber slide. To foster cell reattachment, this subset of samples was incubated for 24 h after cell transfer.

Ultrasound exposure platform: Technical description

To facilitate the application of ultrasound to cell samples, we have developed a custom exposure platform, as illustrated in Figure 1. This three-level acrylic platform was immersed completely in a 37°C degassed water bath. At the bottom level is the ultrasound transducer (facing upward) with 1-MHz frequency and 2.54-cm diameter

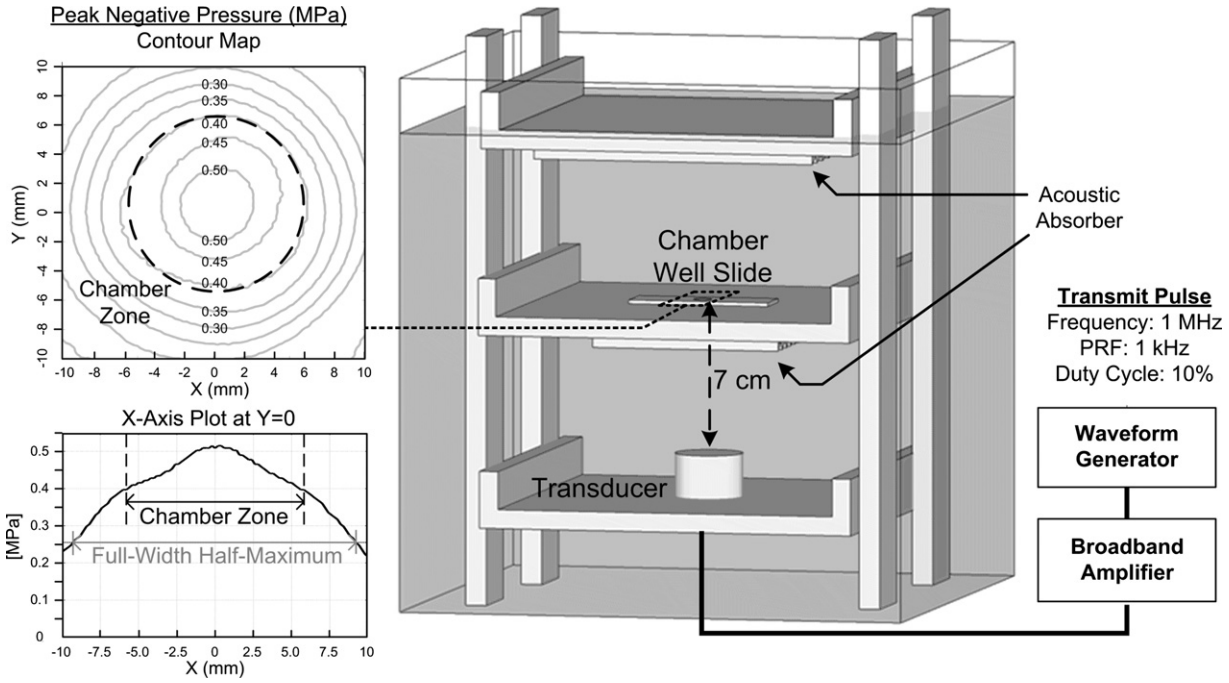

Fig. 1. Schematic of ultrasound exposure platform showing platform components and key acoustic transmission parameters. Upper left inset: Contour map of the peak negative pressure for the cross-sectional area across the chamber well as obtained from hydrophone measurements (each contour step denotes 0.05 MPa). Lower left inset: x-axis plot of the peak negative pressure along the $y = 0$ line. Peak negative pressure within the chamber zone ranged between 0.40 and 0.51 MPa, and the corresponding spatial average was 0.45 MPa. Note that the chamber zone diameter was smaller than the pressure field's full width at half-maximum.

(P1T10W-25; Kunshan Rishun Electronics, Jiangsu, China). The transducer was driven by a signal generator setup that comprised an arbitrary waveform generator (33120A; Agilent Technologies, Santa Clara, CA, USA) and a 50-dB-gain broadband amplifier (2100L; Electronics and Innovation, Rochester, NY, USA). The middle platform level, 7 cm above the transducer, housed the secure-sealed chamber well slide that was mounted upside down with the HybriWell cover facing the transducer (*i.e.,* for the attached cells, the monolayer is positioned at the top of the slide). To help concentrate the ultrasound exposure at the chamber well slide, a 3.2-cm-diameter aperture was drilled at the center of the middle level, and acoustic absorber (facing downward) was padded around the aperture. The upper platform level was positioned 7 cm above the middle level. It was padded with acoustic absorber to prevent ultrasound that reached the top of platform from reflecting back toward the cell sample. This was done to avoid standing waves from emerging, thereby improving the homogeneity of acoustic exposure conditions during operation (Hensel et al. 2011; Leskinen et al. 2012).

Acoustic exposure parameters and calibration

To characterize the in situ ultrasound exposure level, measurements of peak negative pressure were made using a needle hydrophone (HNR-0500; Onda, Sunnyvale, CA, USA) and a three-axis micropositioner (ASTS-01; Onda). In particular, a planar map of the peak negative pressure in the vicinity of the chamber well slide was obtained by taking hydrophone measurements at scan coordinates along the surface of the middle level's aperture (in the absence of the chamber well slide). To account for insertion loss on mounting the chamber well slide, a HybriWell cover (*i.e.,* the slide's transducer-facing side) was mounted across the aperture prior to making the measurements (the hydrophone was calibrated to be 1 mm from this chamber to avoid tip contact). Note that the HybriWell cover is made of polycarbonate, and it is essentially an acoustically thin surface (0.18-mm slab thickness) with respect to the ultrasound wavelength at 1-MHz frequency (1.5 mm). Its acoustic attenuation coefficient was previously reported to be 0.5 dB/(mm·MHz) (Selfridge 1985).

The insets to Figure 1 show the measured peak negative pressure field that was applied in all our experiments. As can be observed, the pressure distribution was relatively homogeneous within the chamber zone (12 mm in diameter) as it was positioned within the pressure field's focal region and was significantly smaller than the field's full width at half-maximum (FWHM) of 18.5 mm. Peak negative pressure values ranged between

0.40 and 0.51 MPa over the planar cross section of the chamber well, and the corresponding spatial average was estimated to be 0.45 MPa. This ultrasound field was applied to each experimental trial in the form of 100-cycle pulses with 1-MHz center frequency. Pulse repetition frequency (PRF) was set at 1 kHz (yielding a 10% duty cycle for our given pulse length), and exposure duration was kept at 60 s. As considered in previous dosage studies on sonoporation (Guzman et al. 2003), these parameters correspond to a spatially averaged acoustic energy density of 41 J/cm^2—a relatively mild ultrasound dosage that would not lead to cellular damage in a microbubble-free medium.

Use of microbubbles to facilitate sonoporation

Commercial lipid-shelled microbubbles (TS-108; Targeson, San Diego, CA, USA) were used to serve as artificial gas nuclei for sonoporation. These microbubbles were 2.09 μm in mean diameter, and less than 1.7% of them were larger than 5 μm (according to the manufacturer's data). They were added just before ultrasound exposure at a concentration corresponding to a 10:1 cell:bubble ratio within the chamber well (for confocal microscopy experiments done on attached cells, time was given to allow the microbubbles to rise to the top of the well slide where the cell monolayer was located). Such a cell:bubble ratio was chosen based on previous findings that demonstrated sonoporation efficiency was higher (*i.e.,* achieving sonoporation while limiting cases of instant cell lysis) when there were more cells than microbubbles in the medium (Guzman et al. 2003). As such, the sonoporated cells in our investigations can generally be assumed to remain viable immediately after exposure (this is an essential experimental control condition for our intended demonstration of sonoporation-induced cellular stress). Note that in our experimental trials, most of the microbubbles were found to have collapsed after exposure (deduced from empirical observations of the chamber well under a bright-field microscope). This suggests that acoustic cavitation (most likely inertial cavitation) had taken place over the exposure period as necessary to facilitate sonoporation. To obtain comparative evidence for such an assertion, a subset of experiments were conducted without adding microbubbles to the medium to determine the cellular impact of mere ultrasound exposure with our specified acoustic settings.

Fluorescence labeling of sonoporated cells with macromolecule uptake

To facilitate tracking of sonoporated cells with enhanced uptake of exogenous molecules, 10 μM calcein fluorescence markers (C481, Invitrogen; absorption FWHM: 475–505 nm; emission FWHM: 500–540 nm) were added to the cell mixture 15 min before ultrasound exposure. This marker, with a molecular weight of 623 Da and molecular radius of 0.65 nm, would normally remain in the extracellular environment unless the cell membrane became permeabilized, as would be the case with sonoporation (Guzman et al. 2002). Their cytoplasmic presence can thus provide an indication that sonoporation has taken place in a cell.

Confocal microscopy: Analysis of post-sonoporation cell morphology

The post-exposure morphology of sonoporated cells was examined using confocal microscopy. We focused particularly on the dynamics of the plasma membrane and intra-cellular lipids. To facilitate this investigation, 8.2 μM FM 4-64 membrane-sensitive fluorescence dye (T3166, Invitrogen; absorption FWHM: 445–565 nm; emission FWHM: 660–815 nm) was loaded onto the cells 1 h before adding calcein and microbubbles. The cells were then exposed to ultrasound using the platform described earlier. Immediately after ultrasound exposure, extracellular calcein was removed by washing with a phosphate-buffered saline (PBS) solution containing 1% fetal bovine serum (replaced with fresh culture medium afterward). The cells were then reincubated for 2 h to foster recovery. After that, they were fixed by adding 4% formaldehyde into the chamber well for 15 min, and their nuclei were stained with 6.5 μM 4',6-diamidino-2-phenylindole) fluorescence dye (DAPI; D1306, Invitrogen; absorption FWHM: 320–388 nm; emission FWHM: 420–512 nm) for 10 min (they were washed with PBS afterward). Subsequently, confocal images of these fixed cells were obtained using a laser scanning confocal microscope (LSM 710; Carl Zeiss, Jena, Germany) equipped with a 63$\times$ objective lens (pixel dwell time was set at 12.6 μs). Given the absorption and emission FWHM of the three fluorescent dyes, the following excitation wavelengths were used: 543 nm (FM 4-64), 350 nm (DAPI) and 488 nm (calcein); the corresponding detection bands were 650–730 nm (FM 4-64), 430–480 nm (DAPI) and 500–550 nm (calcein).

From the confocal images, the intra-cellular lipid level of sonoporated cells was quantified using built-in functions in the ZEN software (Carl Zeiss), and these were compared against those in the sham exposure group. Cellular cross-sectional area was also quantitatively analyzed based on bright-field images acquired with the same instrument. The means and standard errors of these measurements were computed in each population sample (based on a count size of $>$100 cells, repeated for three different trials). Analysis of variance (ANOVA) was performed between exposure groups to identify statistically significant differences.

Flow cytometry: Analysis of cell cycle kinetics of sonoporated cells

Bromodeoxyuridine labeling of S-phase cells. The post-exposure developmental trend of sonoporated cells was quantitatively analyzed using flow cytometry. In particular, the deoxyribonucleic acid (DNA) synthesis kinetics of these cells was evaluated using the 5-bromo-2'-deoxyuridine (BrdU) marker, which binds to cells in the synthesis phase (S phase) of the cell cycle. For this part of the investigation, pre-exposure cells (prior to addition of calcein and microbubbles) were first pulsed with 10 μM BrdU markers (550891; BD Biosciences, Franklin Lakes, NJ, USA) for 30 min to label cells that were in S phase at that time. Unbound BrdU was removed by washing the cells with warm complete culture medium, after which the cells were exposed to ultrasound based on the protocol described earlier. Cells were taken out of the chamber immediately after exposure and were washed with PBS (containing 1% fetal bovine serum) to remove extracellular calcein. Subsequently, they were transferred to a round culture dish (430167; Corning, Corning, NY, USA) for reincubation within a 37°C, 5% CO_2 environment.

Sorting of viable sonoporated cells. At three post-exposure time points (0, 3 and 6 h), cells were extracted for flow cytometry analysis (5×10^6 cells were harvested for each experimental run). Non-viable cells were first labeled using 75 μM propidium iodide (PI) (P4170, Sigma–Aldrich; absorption maximum: 488 nm; emission maximum: 630 nm), which was added 15 min before performing flow cytometry. After that, bivariate

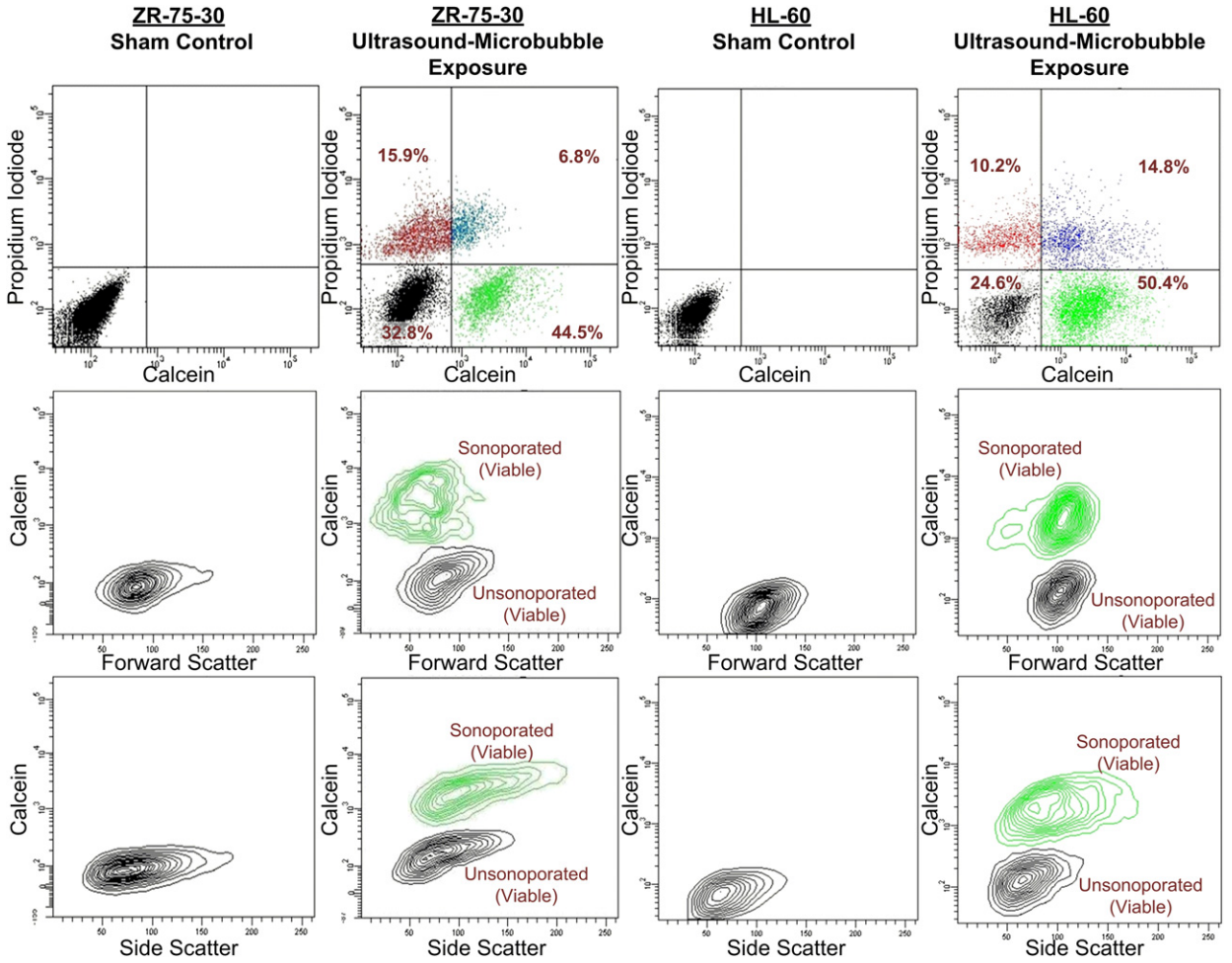

Fig. 2. Flow cytometry analysis of sonicated cells performed 3 h after exposure. Data for sham controls are provided in columns 1 and 3, respectively, for ZR-75-30 and HL-60 cells. Results of sonication are given in columns 2 and 4 for the two cell types (1-MHz frequency, 1-kHz PRF, 100-cycle pulse length, 0.45-MPa spatially averaged peak negative pressure, 60-s duration, 10:1 cell:bubble ratio). In row 1 are bivariate plots of the distributions of cells that are viable (stained by PI) and sonoporated (calcein uptake). In rows 2 and 3, respectively, are the forwardscatter and sidescatter distributions of viable unsonoporated (black) and sonoporated cells (green).

calcein/PI fluorescence analysis of the cells was carried out in a flow cytometer (FACSAriaa III, BD Biosciences) that sorted cells at the rate of 3000 events/s (excitation wavelength was 488 nm for both markers, whereas detection bands were 616 ± 23 and 530 ± 30 nm, respectively, for PI and calcein). This served to extract sonoporated cells that remained viable after exposure for further analysis of their DNA synthesis kinetics with BrdU flow cytometry. As shown in row 1 of Figure 2 (see columns 2 and 4), for both cell types, viable sonoporated cells (*i.e.,* calcein positive and PI negative) accounted for between 45 and 50% of the sonicated cell population. Their forward-scatter (FSC) and side-scatter (SSC) distributions were analyzed to obtain supplementary evidence respectively on cell size and cellular granularity.

Analysis of BrdU-labeled sonoporated cells. The DNA synthesis kinetics of viable sonoporated cells was investigated using the BrdU/DNA flow cytometry analysis technique (Begg et al. 1985). In carrying out this task, the sorted cells were first fixed with ice-cold ethanol and stored at −20°C overnight, after which they were centrifuged to remove supernatants and washed with PBS. Cell sample DNA was partially denatured by incubating the cells with 2 M hydrogen chloride for 20 min at room temperature (washed three times afterward with PBS containing 0.05% Tween-20 surfactants). Next, BrdU-positive cells (*i.e.,* S-phase cells just before exposure) were fluorescently labeled by incubating the cells first with 100 μL of 1:50 anti-BrdU monoclonal antibody (555627, BD Biosciences) for 1 h and then with 100 μL of 1:100 Alexa Fluor 647 conjugated goat anti-mouse IgG antibody (A21235, Invitrogen; absorption maximum: 650 nm; emission maximum: 668 nm) for 30 min in the dark. Subsequently, the cells were stained with PI for 15 min to label their DNA contents (note that the cells were PI negative before fixation, and that this latter PI staining was for labeling of the fixed cells' DNA rather than identification of non-viable cells). After that, BrdU/DNA bivariate scatter plots of these cells were obtained using the flow cytometer to facilitate time-course analysis of DNA synthesis for viable sonoporated cells that were in S phase just before ultrasound exposure. An excitation wavelength of 633 nm and a detection band of 660 ± 20 nm were used for fluorescence activation of BrdU-positive cells (same parameters as before were used for PI). From these plots, the temporal progression of DNA synthesis of BrdU-positive cells was examined, and DNA synthesis time was estimated using the relative movement extrapolation method as described elsewhere (Begg et al. 1985). Inter-group statistics (with $N = 4$) were then compared using the Student's *t*-test to identify significant differences.

RESULTS

Membrane shrinkage in sonoporated cells over time

Sonoporated cells (2 h after exposure) were found to exhibit morphological differences as compared with sham-exposed cells and cells that remained unsonoporated after ultrasound-microbubble exposure. Confocal microscopy images corresponding to this finding are shown in Figure 3 for ZR-75-30 attached cells. As can be observed, one distinct morphological feature of sonoporated cells (*i.e.,* calcein positive; see Fig. 3c) is that they seem to have shrunk in size. Indeed, rounding of both membrane and cell nucleus is evident as a result of sonoporation. It is worth noting that post-exposure membrane resealing likely took place in these sonoporated cells, as their plasma membrane (labeled with FM 4-64) were found to be intact.

Size reduction observed in sonoporated cells

Likely as a consequence of the post-exposure membrane shrinkage phenomenon, sonoporated cells were found to be smaller 2 h after exposure. Figure 4a illustrates a statistical analysis of cellular cross-sectional area for different cell groups. There is a significant decrease in the average size of sonoporated cells (61% decrease in cross-sectional area). This is consistent with the flow cytometry results shown in Figure 2 (see row 2, columns 1 and 2) that depicted a drop in the viable sonoporated cells' FSC distribution, which is typical of a cell size decrease. Note that a post-exposure reduction in cell size may also be observed to a lesser extent for unsonoporated cells that were sonicated in the presence of microbubbles (*i.e.,* cells in Fig. 3b). This suggests that even though membrane permeation was not realized on these cells, the cavitational force resulting from ultrasound–microbubble interactions may still be substantial enough to induce stress on cells.

Lipid accumulation within sonoporated cells

Another noteworthy morphological feature of sonoporated cells is their increased intra-cellular lipid level. As evidenced by the higher FM 4-64 fluorescence within the cellular membrane (see Fig. 3c), sonoporation gives rise to an accumulation of lipids in the cytoplasm that appear vacuolar-like. This is summarized in Figure 5a, which shows that sonoporated cells exhibited a rise in intra-cellular FM 4-64 fluorescence (381% higher than that of sham control cells). It is in line with the flow cytometry plots in Figure 2 (see row 3, columns 1 and 2) that showed an increase in the sonoporated cells' SSC distribution as reflective of a rise in cellular granularity. Note that the lipids accumulated within the cytoplasm and not at the membrane interface. Hence, this phenomenon is unlikely to be connected to

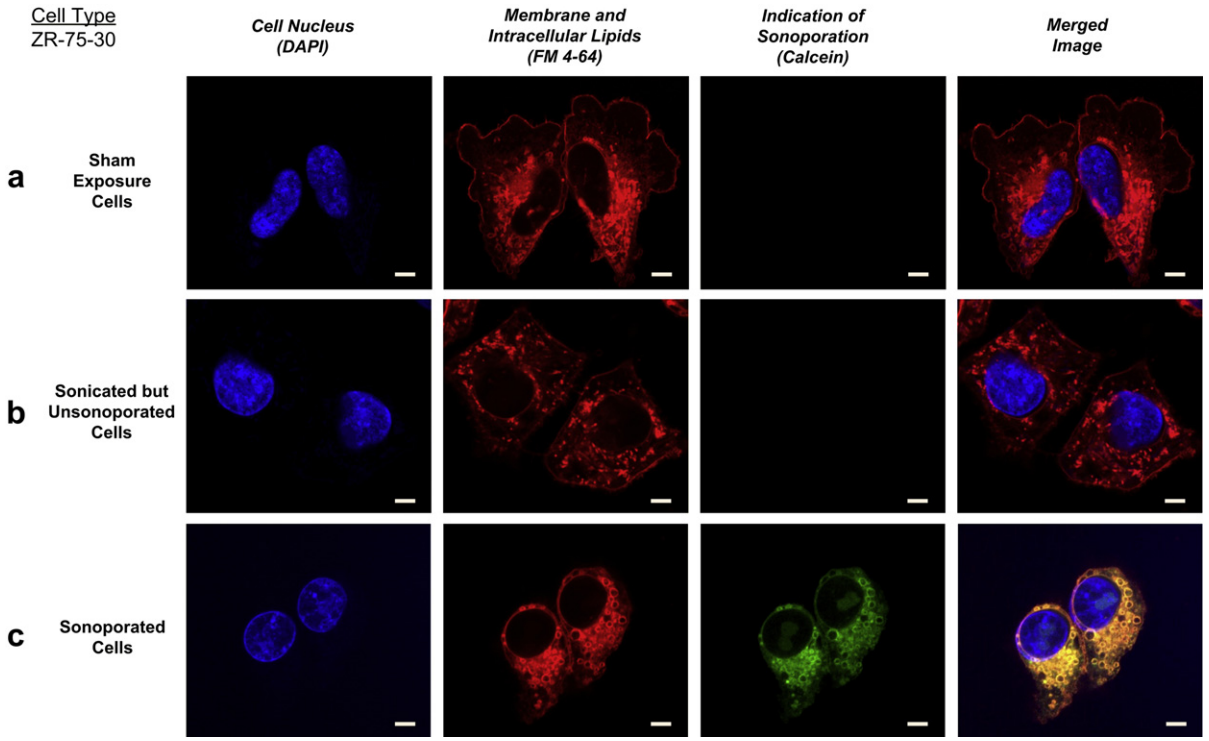

Fig. 3. Confocal microscopy images of ZR-75-30 attached cells showing sonoporation-induced morphological repression. Each row contains images for (a) sham-exposed cells; (b) cells that remained unsonoporated after ultrasound–microbubble exposure; and (c) sonoporated cells. Ultrasound exposure parameters are the same as those in Figure 2. In column 1, blue indicates nucleus (DAPI); in column 2, red indicates plasma membrane and lipid contents (FM 4-64); and in column 3, green indicates sonoporation (calcein). Merged fluorescence images are shown in column 4. Bar = 5 μm. Note: Data for cells sonicated in the absence of microbubbles are not shown (their morphology is similar to that of sham-exposed cells).

membrane resealing that should have already taken place seconds after exposure. Instead, it may be indicative of a disruption to the normal course of intra-cellular lipid metabolism.

Similarity of sonoporated cell morphology among cell types

The repressive morphological characteristics observed in sonoporated ZR-75-30 attached cells can also

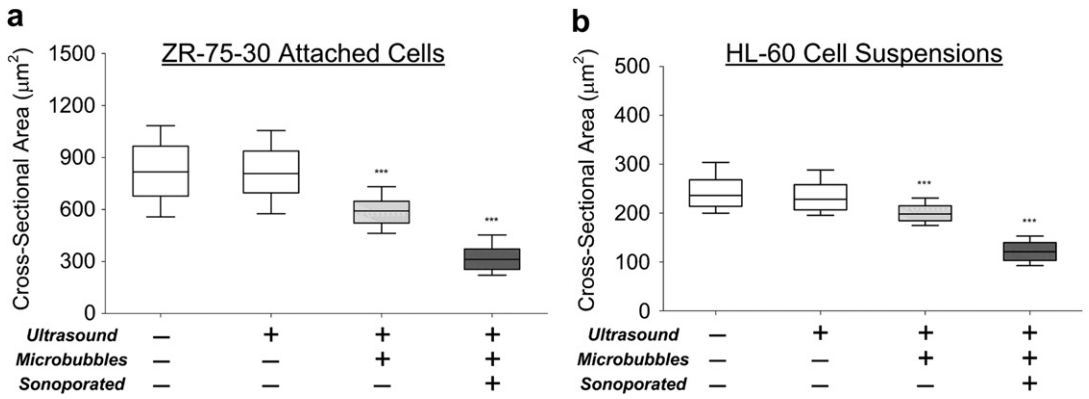

Fig. 4. Sonoporated cells exhibited a reduction in cellular cross-sectional area as compared with sham-exposed cells. Box plots are shown for the following cell types: (a) ZR-75-30 attached cells and (b) HL-60 cell suspensions ($N = 3$, each estimate averaged from >100 cells in a population sample). Four cell groups were considered: sham-exposed cells (left); sonoporated cells (right); unsonoporated cells after ultrasound exposure in the absence or presence of microbubbles (two middle boxes). ***$p < 0.001$.

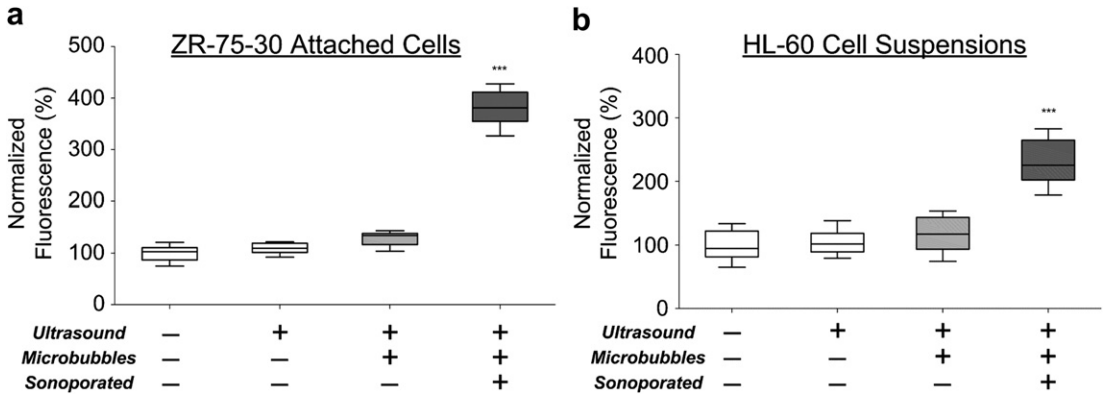

Fig. 5. Increase in intra-cellular lipid content of sonoporated cells, as indicated by an increase in FM 4-64 fluorescence. Data are shown in the form of box plots for (a) ZR-75-30 attached cells and (b) HL-60 cell suspensions. Measurements are expressed as percentages (normalized with respect to the mean baseline level for sham-exposed cells). In each plot, the four boxes respectively show results for sham exposure cells (left); sonoporated cells (right); and unsonoporated cells after ultrasound exposure in the absence or presence of microbubbles (two middle boxes). $***p < 0.001$. $N = 3$ (each estimate averaged from >100 cells).

be found in HL-60 cell suspensions. Confocal images corresponding to this finding are shown in Figure 6, which compares cellular features between sonoporated and control cells. As noted from these images, sonoporated HL-60 cells exhibited both membrane shrinkage and intra-cellular lipid accumulation. This is supported by the quantitative measurements shown in Figures 4b and 5b that showed a 50% reduction in sonoporated cell size and a 231% increase in intra-cellular FM 4-64 fluorescence level, respectively. Similar observations can be noted for the FSC and SSC distributions of viable sonoporated cells shown in Figure 2 (see columns 3 and 4, rows 2 and 3). In particular, these cells exhibited a relative decrease in FSC (related to cell size) and an increase in SSC (related to cell granularity).

Cell cycle progression delays in viable sonoporated cells

Our flow cytometry results indicate that not only are repressive morphological changes observed in sonoporated cells, delays in their cell cycle progression are evident as well. As shown in Figure 7 for both ZR-75-30 and HL-60 cell types, viable sonoporated cells originally in the S phase of the cell cycle (*i.e.,* BrdU positive) exhibited delayed completion of their DNA synthesis process. This can be noted by observing that

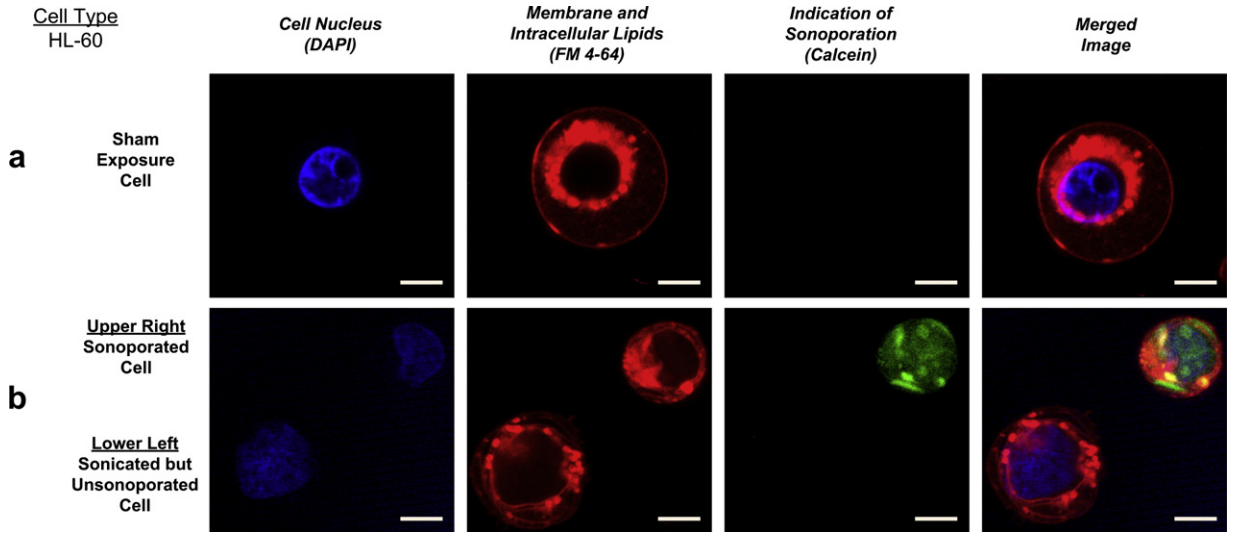

Fig. 6. Confocal microscopy images of HL-60 cell suspensions showing a trend toward sonoopration-induced morphological repression similar to that observed for ZR-75-30 cells. Bar = 5 μm. (a) Sham-exposed cell; (b) unsonoporated cell (bottom left) and sonoporated cell (upper right) within the same image (both were exposed to ultrasound–microbubble treatment identical to that in Fig. 2). Interpretation of fluorescence colors is the same as in Figure 3.

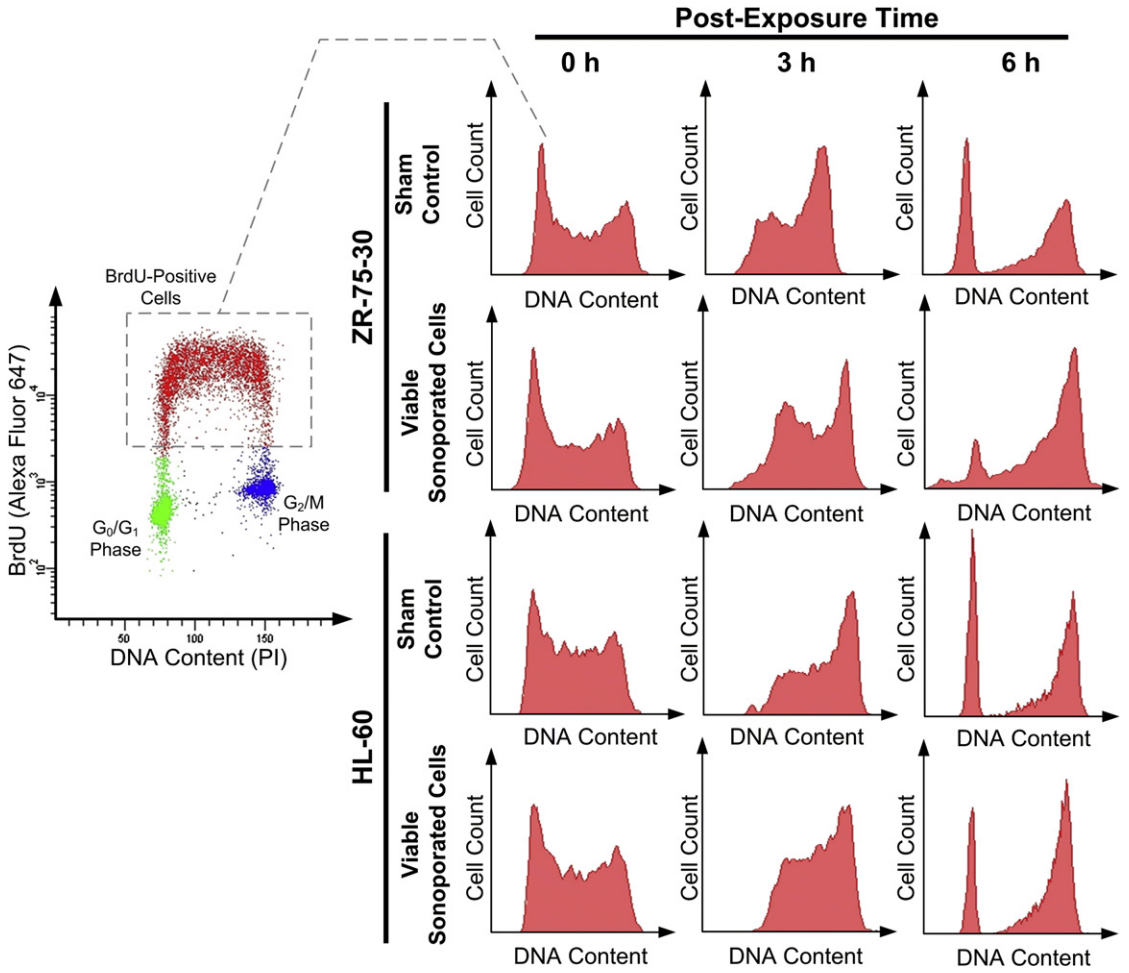

Fig. 7. Delayed cell cycle progression of viable sonoporated cells as determined from BrdU/DNA flow cytometry. Left: Representative BrdU/DNA bivariate scatter plot illustrating how BrdU-positive cells (*i.e.,* cells in S phase of cell cycle before exposure) were identified for DNA content analysis. Right: Series of DNA histograms for BrdU-positive cells at three post-exposure time points (0, 3 and 6 h). Rows 1 and 2 show results for ZR-75-30 cells in the sham-exposed group and viable sonoporated cell group (based on same exposure parameters as used in Fig. 2). In rows 3 and 4, corresponding results are shown for HL-60 suspensions.

in the DNA histograms of these cells (rows 2 and 4), in comparison to those for sham exposure (rows 1 and 3), there is a slower temporal shift toward the right peak, the magnitude of which reflects the number of cells that had completed DNA synthesis and entered the G_2/M (gap 2 or mitosis) phase of the cell cycle.

In a related observation, according to the DNA histograms, at 6 h after exposure (right column of Fig. 7), a significantly smaller fraction of BrdU-positive sonoporated cells had completed their mitosis and returned to the G_0/G_1 (gap 0 or gap 1) phase of the cell cycle. This is reflected by the smaller left peak in the DNA histograms of BrdU-positive sonoporated cells. On average, as plotted in Figure 8a for ZR-75-30 cells, only 4.3% of BrdU-positive sonoporated cells were in the post-mitotic phase 6 h after exposure (as compared with 17.6% of BrdU-positive sham -exposed cells). A similar trend can be observed for HL-60 cells (see Fig. 8b): 11.1% of BrdU-positive sonoporated cells had returned to the G_0/G_1 phase (in comparison to 18.8% of BrdU-positive sham-exposed cells).

Significantly lengthened DNA synthesis time of sonoporated cells

By quantitatively analyzing the flow cytometry plots shown in Figure 7 *via* the BrdU relative movement extrapolation technique (Begg et al. 1985), we found that the DNA synthesis time of sonoporated cells was significantly lengthened. Results corresponding to this observation are summarized in Figure 9, which compares the DNA synthesis times of BrdU-positive sham-exposed cells and BrdU-positive sonoporated cells. Note that for ZR-75-30 attached cells, there is a 250% increase (6.2 h for control vs. 15.2 h for sonoporated cells) in the

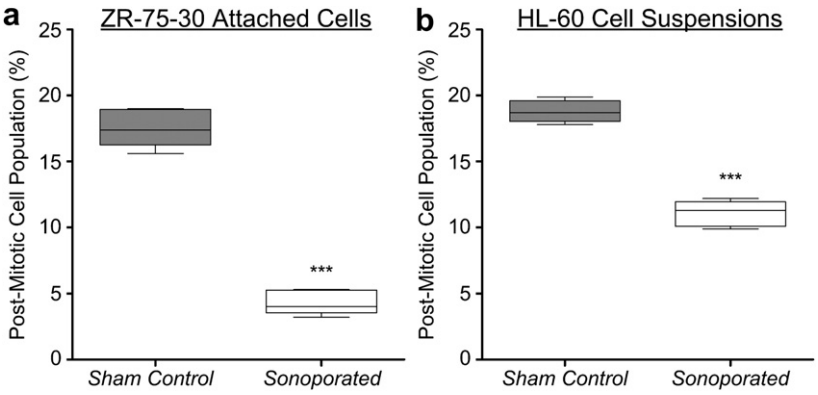

Fig. 8. Reduction in the post-mitotic population of BrdU-positive cells as a result of sonoporation. Box plot results for ZR-75-30 attached cells (a) and HL-60 cell suspensions (b). $N = 4$. $***p < 0.001$.

estimated duration of DNA synthesis as a result of sonoporation. This repressive impact varies between cell types. The increase in DNA synthesis duration was less substantial for HL-60 cell suspensions (8.7 h for control cells vs. 13.4 h for sonoporated cells, *i.e.,* 154% increase), but was still statistically significant.

DISCUSSION

Integrated perspective of results

In considering sonoporation as a membrane permeation strategy for drug/gene delivery applications, its biological aspects have often been overlooked. In this work, we sought to address this knowledge gap by investigating the morphological characteristics and developmental kinetics of sonoporated cells with enhanced exogenous molecule uptake (calcein fluorescence markers in our case). Through confocal microscopy observations and flow cytometry assays, we generally found that sonoporation, although capable of facilitating internalization of exogenous molecules, may inadvertently elicit a cellular stress response.

One indication of sonoporation-induced cellular stress is the emergence of repressive morphological characteristics presumably after membrane resealing occurred. In particular, over a multi-hour time frame (2 h in our study), sonoporated cells would exhibit membrane shrinkage and intra-cellular accumulation of lipids (Figs. 3–6). As known from cell biology, both morphological characteristics are connected to cellular stress. First, membrane shrinkage has been regarded as part of an apoptotic volume decrease resulting from disrupted transmembranous ion transfer kinetics (Bortner and Cidlowski 2007; Hoffman and Pedersen 2011)—a phenomenon that sonoporation is known to induce by triggering Ca^{2+} influx (Fan et al. 2010; Kumon et al. 2009; Park et al. 2010; Tsukamoto et al. 2011) and potassium ion (K^{+}) efflux (Juffermans et al. 2008; Tran et al. 2008). Second, intra-cellular lipid accumulation signifies the presence of disrupted lipid metabolism, an event that has already been demonstrated to occur in perforated cells (Gurcel et al. 2006). Considered as a stress on the endoplasmic reticulum (*i.e.,* the subcellular organelle responsible for protein folding), such

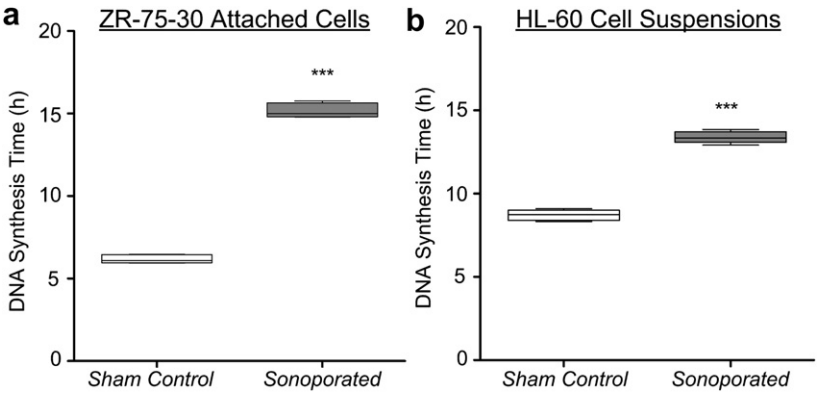

Fig. 9. Sonoporated cells exhibit lengthening of DNA synthesis time as determined from relative movement analysis of BrdU/DNA flow cytometry plots. Results for both sham-exposed cells and sonoporated cells are shown in the form of box plots for (a) ZR-75-30 attached cells and (b) HL-60 cell suspensions. $***p < 0.001$ (for $N = 4$).

a phenomenon may be the result of different effects including the triggering of unfolded protein response (Ron and Walter 2007) and resealing-induced endocytosis (Idone et al. 2008).

On further analysis of sonoporated cells using flow cytometry, we found that these cells are indeed under stress from the perspective of cellular development. Specifically, our BrdU cell cycle progression assay revealed that the pace at which sonoporated cells progress through cell cycle was significantly hindered (Figs. 7 and 8). Depending on cell type, the DNA synthesis time was found to be lengthened by up to 250% (Fig. 9). This is consistent with well-accepted cell wounding principles in the biology literature that suggests the need for injured cells to undergo internal recovery before they resume proliferation (Branzei and Foiani 2008).

Implications of findings

As our findings generally point to the existence of sonoporation-induced cellular stress, they seem to echo a recent statistical analysis (Liu et al. 2012) that called for reconsideration of efficiency issues (*i.e.,* achieving membrane permeation without disrupting cellular homeostasis) in using sonoporation for drug/gene delivery purposes. To further understand the factors limiting sonoporation efficiency, it would be of interest to connect the stress response observed in this study and the cellular mechanism of membrane structural changes in sonoporation. One particular follow-up investigation that is worth pursuing is determining how sonoporation-induced transmembranous trafficking of bioelectrical ions (not limited to Ca^{2+} influx) and liposomal vesicles (hypothesized to play an active role in membrane resealing) would contribute to instigation of a cellular stress response. Establishing this mechanistic connection would provide a more detailed account of the sequence of biological events involved in sonoporation.

In addition to their relevance to the optimization of sonoporation-mediated drug/gene delivery, our experimental findings may provide new perspectives on the therapeutic potential of sonoporation. For instance, one possible direction that may be explored is the development of new sonoporation-mediated treatment paradigms involving intentional induction of cellular injury with emphasis on temporarily halting cellular development. Inhibition of cancerous cell growth would be one potential application fitting into this treatment strategy. It can likely be combined with the delivery of anti-cancer drugs to take advantage of the increased membrane permeability facilitated by sonoporation (note that the feasibility of sonoporation-enhanced anti-cancer drug uptake has already been confirmed [Matsuo et al. 2011; Sasaki et al. 2012]). Such a hybrid treatment paradigm may represent a more synergistic way of leveraging sonoporation for biomedical applications.

CONCLUSION

As a biophysical phenomenon with potential in facilitating drug/gene delivery, sonoporation has already attracted significant interest within the biomedical community. Although much effort has been devoted to realizing this biophysical phenomenon through innovations in microbubble design and physical analysis of ultrasound dosages, a fundamental understanding of its associated cellular response remains to be established. The findings reported here, namely, those on the morphological response and developmental kinetics of sonoporated cells, essentially represent new insight into how sonoporation may stress cells even though their viability remains unaffected. Our findings were obtained under *in vitro* settings, and thus it would be worthwhile to extend this investigation to *in vivo* scenarios to more directly evaluate the repressive impact of sonoporation in practical applications. From a biophysical standpoint, additional studies are also needed to correlate the details of acoustic cavitation (*e.g.,* type, magnitude) with the induction of repressive characteristics in sonoporated cells. We anticipate that with enriched efforts in investigating the biological aspects of sonoporation, proper cytoprotection strategies may be developed to reinforce the efficacy of sonoporation-mediated drug/gene delivery; in addition, further innovations in sonoporation-based treatment applications may be formulated.

Acknowledgments—This work has been supported in part by the Hong Kong Innovation and Technology Fund (ITS/292/11) and the University of Hong Kong (201109176229). The authors are grateful to Dr. Wai-Hung Sit for his technical advice on the bromodeoxyuridine flow cytometry assay.

REFERENCES

Begg AC, McNally NJ, Shrieve DC, Karcher H. A method to measure the duration of DNA synthesis and the potential doubling time from a single sample. Cytometry 1985;6:620–626.

Bortner CD, Cidlowski JA. Cell shrinkage and monovalent cation fluxes: Role in apoptosis. Arch Biochem Biophys 2007;462:176–188.

Branzei D, Foiani M. Regulation of DNA repair throughout the cell cycle. Nat Rev Mol Cell Biol 2008;9:297–308.

Campbell P, Prausnitz MR. Future directions of therapeutic ultrasound. Ultrasound Med Biol 2007;33:657.

Chen YC, Liang HD, Zhang QP, Blomley MJK, Lu QL. Pluronic block copolymers: Novel functions in ultrasound-mediated gene transfer and against cell damage. Ultrasound Med Biol 2006;32:131–137.

Fan Z, Kumon RE, Park J, Deng CX. Intracellular delivery and calcium transients generated in sonoporation facilitated by microbubbles. J. Control Release 2010;142:31–39.

Feril LB Jr, Kondo T. Biological effects of low intensity ultrasound: The mechanism involved, and its implications on therapy and on biosafety of ultrasound. J Radiat Res 2004;45:479–489.

Frenkel V. Ultrasound mediated delivery of drugs and genes to solid tumors. Adv Drug Deliv Rev 2008;60:1193–1208.

Gurcel L, Abrami L, Giradin S, Tschopp J, van der Goot FG. Capase-1 activation of lipid metabolic pathways in response to bacterial pore-forming toxins promotes cell survival. Cell 2006;126:1135–1145.

Guzman HR, McNamara AJ, Nguyen DX, Prausnitz MR. Bioeffects caused by changes in acoustic cavitation bubble density and cell concentration: A unified explanation based on cell-to-bubble ratio and blast radius. Ultrasound Med Biol 2003;29:1211–1222.

Guzman HR, Nguyen DX, Mcnamara AJ, Prausnitz MR. Equilibrium loading of cells with macromolecules by ultrasound: Effects of molecular size and acoustic energy. J Pharm Sci 2002;91:1693–1701.

Hassan MA, Campbell P, Kondo T. The role of Ca^{2+} in ultrasound-elicited bioeffects: Progress, perspectives and prospects. Drug Discov Today 2010;15:892–906.

Hensel K, Mienkina MP, Schmitz G. Analysis of ultrasound fields in cell culture wells for in vitro ultrasound therapy experiments. Ultrasound Med Biol 2011;37:2105–2115.

Hoffmann EK, Pedersen SF. Cell volume homeostatic mechanisms: Effectors and signaling pathways. Acta Physiol 2011;202:465–485.

Hutcheson JD, Schlicher RK, Hicks HK, Prausnitz MR. Saving cells from ultrasound-induced apoptosis: Quantification of cell death and uptake following sonication and effects of targeted calcium chelation. Ultrasound Med Biol 2010;36:1008–1021.

Idone V, Tam C, Andrews NW. Two-way traffic on the road to plasma membrane repair. Trends Cell Biol 2008;18:552–559.

Juffermans LJM, Kamp O, Dijkmans PA, Visser CA, Musters RJP. Low-intensity ultrasound-exposed microbubbles provoke local hyperpolarization of the cell membrane via activation of BK_{Ca} channels. Ultrasound Med Biol 2008;34:502–508.

Karshafian R, Samac S, Bevan PD, Burns PN. Microbubble mediated sonoporation of cells in suspension: Clonogenic variability and influence of molecular size on uptake. Ultrasonics 2010;50:691–697.

Kumon RE, Aehle M, Sabens D, Parikh P, Han YW, Kourennyi D, Deng CX. Spatiotemporal effects of sonoporation measured by real-time calcium imaging. Ultrasound Med Biol 2009;35:494–506.

Leskinen J, Hynynen K. Study of factors affecting the magnitude and nature of ultrasound exposure with in vitro set-ups. Ultrasound Med Biol 2012;38:777–794.

Liu Y, Yan J, Prausnitz MR. Can ultrasound enable efficient intracellular uptake of molecules? A retrospective literature review and analysis. Ultrasound Med Biol 2012;38:876–888.

Matsuo M, Yamaguchi K, Feril LB Jr, Endo H, Ogawa K, Tachibana K, Nakayama J. Synergistic inhibition of malignant melanoma proliferation by melphalan combined with ultrasound and microbubbles. Ultrason Sonochem 2011;18:1218–1224.

Mehier-Humbert S, Bettinger T, Yan F, Guy R. Influence of polymer adjuvants on the ultrasound-mediated transfection of cells in culture. Eur J Pharm Biopharm 2009;72:567–573.

Miller DL, Dou C. Induction of apoptosis in sonoporation and ultrasonic gene transfer. Ultrasound Med Biol 2009;35:144–154.

Miller DL, Pislaru SV, Greenleaf JE. Sonoporation: Mechanical DNA delivery by ultrasonic cavitation. Somat Cell Mol Genet 2002;27:115–134.

Park J, Fan F, Kumon RE, El-Sayed MEH, Deng CX. Modulation of intracellular Ca^{2+} concentration in brain microvascular endothelial cells in vitro by acoustic cavitation. Ultrasound Med Biol 2010;36:1176–1187.

Pua EC, Zhong P. Ultrasound-mediated drug delivery. IEEE Eng Med Biol Mag 2009;28:64–75.

Qiu Y, Luo Y, Zhang Y, Cui W, Zhang D, Wu J, Zhang J, Tu J. The correlation between acoustic cavitation and sonoporation involved in ultrasound-mediated DNA transfection with polyethylenimine (PEI) in vitro. J Control Release 2010;145:40–48.

Ron D, Walter P. Signal integration in the endoplasmic reticulum unfolded protein response. Nat Rev Mol Cell Biol 2007;8:519–529.

Sasaki N, Kudo N, Nakamura K, Lim SY, Murakami M, Kumura WRB, Tamura Y, Ohta H, Yamasaki M, Takiguchi M. Activation of microbubbles by short-pulsed ultrasound enhances the cytotoxic effect of *cis*-diamminedichloroplatinum (II) in a canine thyroid adenocarcinoma cell line in vitro. Ultrasound Med Biol 2012;38:109–118.

Schlicher RK, Hutcheson JD, Radhakrishna H, Apkarian RP, Prausnitz MR. Changes in cell morphology due to plasma membrane wounding by acoustic cavitation. Ultrasound Med Biol 2010;36:677–692.

Selfridge AR. Approximate material properties in isotropic materials. IEEE Trans Sonics Ultrason 1985;32:381–394.

Sirsi SR, Borden MA. Microbubble compositions, properties and biomedical applications. Bubble Sci Technol 2009;1:3–17.

Tran TA, le Guennec JY, Bougoux P, Tranquart F, Bouakaz A. Characterization of cell membrane response to ultrasound activated microbubbles. IEEE Trans Ultrason Ferroelec Freq Contr 2008;55:44–49.

Tsukamoto A, Higashiyama S, Yoshida K, Watanabe Y, Furukawa KS, Ushida T. Stable cavitation induces increased cytoplasmic calcium in L929 fibroblasts exposed to 1-MHz pulsed ultrasound. Ultrasonics 2011;51:982–990.

Zhong W, Sit WH, Wan JMF, Yu ACH. Sonoporation induces apoptosis and cell cycle arrest in human promyelocytic leukemia cells. Ultrasound Med. Biol 2011;37:2149–2159.

Zhou Y, Shi J, Cui J, Deng CX. Effects of extracellular calcium on cell membrane resealing in sonoporation. J Control Release 2008;126:34–43.

Zhou Y, Yang K, Cui J, Ye JY, Deng CX. Controlled permeation of cell membrane by single bubble acoustic cavitation. J Control Release 2012;157:103–111.